



Speckle-dependent accuracy in phase-sensitive optical coherence tomography

MATT S. HEPBURN,^{1,2,*}  KEN Y. FOO,^{1,2}  PHILIP WIJESINGHE,^{1,3}  PETER R. T. MUNRO,^{2,4}  LIXIN CHIN,^{1,2} AND BRENDAN F. KENNEDY^{1,2,5}

¹*BRITelab, Harry Perkins Institute of Medical Research, QEII Medical Centre, Nedlands, Western Australia, 6009, Australia and Centre for Medical Research, The University of Western Australia, Crawley, Western Australia, 6009, Australia*

²*Department of Electrical, Electronic & Computer Engineering, School of Engineering, The University of Western Australia, 35, Stirling Highway, Perth, Western Australia, 6009, Australia*

³*Current address: SUPA, School of Physics and Astronomy, University of St. Andrews, KY16 9SS, UK*

⁴*Department of Medical Physics and Biomedical Engineering, University College London, Gower Street, London WC1E 6BT, UK*

⁵*Australian Research Council Centre for Personalised Therapeutics Technologies, Australia*

**matt.hepburn@research.uwa.edu.au*

Abstract: Phase-sensitive optical coherence tomography (OCT) is used to measure motion in a range of techniques, such as Doppler OCT and optical coherence elastography (OCE). In phase-sensitive OCT, motion is typically estimated using a model of the OCT signal derived from a single reflector. However, this approach is not representative of turbid samples, such as tissue, which exhibit speckle. In this study, for the first time, we demonstrate, through theory and experiment that speckle significantly lowers the accuracy of phase-sensitive OCT in a manner not accounted for by the OCT signal-to-noise ratio (SNR). We describe how the inaccuracy in speckle reduces phase difference sensitivity and introduce a new metric, speckle brightness, to quantify the amount of constructive interference at a given location in an OCT image. Experimental measurements show an almost three-fold degradation in sensitivity between regions of high and low speckle brightness at a constant OCT SNR. Finally, we apply these new results in compression OCE to demonstrate a ten-fold improvement in strain sensitivity, and a five-fold improvement in contrast-to-noise by incorporating independent speckle realizations. Our results show that speckle introduces a limit to the accuracy of phase-sensitive OCT and that speckle brightness should be considered to avoid erroneous interpretation of experimental data.

© 2021 Optical Society of America under the terms of the [OSA Open Access Publishing Agreement](#)

1. Introduction

Phase-sensitive optical coherence tomography (OCT) is widely used to measure motion in a range of techniques such as Doppler OCT [1] and optical coherence elastography (OCE) [2]. These techniques are increasingly used in biomedical applications including ophthalmology [3–5] and oncology [6–8]. In phase-sensitive OCT, the phase difference between OCT signals acquired at two time points from the same spatial location is calculated either between A-scans [9–12], B-scans [13–15], or volumetric scans [16] to estimate axial displacement or velocity. Phase difference can be used, for example, to estimate blood and lymph flow velocity in Doppler OCT [9,17–22], or to measure mechanical deformation in OCE [23–25]. In addition, phase-sensitive OCT has been used to study the mechanics of the inner ear [26,27] and to develop new OCT contrast mechanisms in magnetomotive [28–30], photothermal [31–33] OCT. Changes in phase measurements are also used in parametric techniques such as polarization-sensitive OCT [34–36].

Importantly, the efficacy of these techniques is largely determined by the precision and accuracy of the phase difference measurement, where precision is typically defined as the spread between

multiple measurements from the same location over time and accuracy is defined as how close measurements are to the true value [37]. In phase-sensitive OCT, precision (*i.e.*, sensitivity to motion) has been extensively characterized in the context of specular reflections by considering optical noise [38–40], however, relatively little attention has been given to accuracy. In fact, in previous studies, precision has been used as a measure of accuracy, which was assumed to be solely proportional to the OCT signal-to-noise ratio (SNR) at that location. This is because in a specular reflection, optical noise is the main source of error, which is typically zero-mean [12,41]. This assumption has been extrapolated to turbid samples, such as tissue. However, as OCT is a coherent imaging modality, the OCT signal in turbid samples gives rise to speckle [42]. Speckle is typically described as bright or dark, corresponding to regions of relatively high intensity (constructive interference) or relatively low intensity (destructive interference) in OCT images, respectively. Whilst the effect of signal decorrelation on sensitivity has been analyzed in speckle [43], the current noise models do not describe how speckle affects accuracy in phase-sensitive OCT. As a result, it remains challenging to optimize image quality in applications involving turbid samples.

In this study, for the first time, we demonstrate how speckle affects the accuracy of phase-sensitive OCT. Firstly, using a linear systems model, we show that even in the absence of optical noise, *i.e.*, infinite OCT SNR, phase difference error is non-zero in speckle, which we show is related to the degree of local interference. Secondly, we describe how the inaccuracy resulting from speckle affects the distribution of phase difference measurements. To quantify speckle-induced inaccuracy, we introduce a new metric, *speckle brightness*, to estimate the degree of constructive interference at a given location in an OCT image. Using Monte Carlo modeling, we show that speckle brightness severely affects sensitivity independent of OCT SNR. For instance, we demonstrate a three-fold degradation in phase difference sensitivity in dark speckle over bright speckle with identical OCT SNR. We validate our theoretical analysis with close correspondence with experimental measurements. Furthermore, we demonstrate that the degradation in sensitivity is dependent on the magnitude of sample motion. Finally, to provide a practical application of our analysis, we demonstrate how consideration of speckle-dependent accuracy can improve compression OCE measurements. By averaging 100 independent speckle realizations to reduce the impact of speckle on phase difference sensitivity, we demonstrate a ten-fold improvement in strain sensitivity in a homogeneous phantom, and a five-fold increase in the contrast-to-noise ratio of a phantom containing a stiff inclusion. Our results demonstrate that speckle has a significant impact on the accuracy of phase-sensitive OCT, and that OCT SNR alone is insufficient to explain the distribution of phase difference measurements in speckle. This suggests that speckle brightness should be considered when analyzing and interpreting phase-sensitive OCT results, and when designing phase-sensitive OCT systems and experiments.

2. Background

2.1. Phase difference error in speckle

In this section, we illustrate the origin of phase difference error in speckle and demonstrate that, even for infinite OCT SNR, phase difference error can be non-zero. We model the OCT signal in the axial direction as a point-spread function (PSF) convolved with a field of point scatterers. Details of the OCT complex PSF [44], and how to determine displacement from the phase difference between OCT scans at the same location [12] are provided elsewhere but are summarized here for completeness. The one-dimensional (1-D) OCT PSF is given by [45]:

$$h(z) = A_0 \exp\left(-2\frac{z^2}{w_z^2}\right) \exp(-2ik_0z), \quad (1)$$

where A_0 is a scaling factor for the amplitude; w_z is the $1/e^2$ resolution of the OCT field amplitude; k_0 is the central wavenumber of the OCT source, $k_0 = 2\pi/\lambda_0$; and λ_0 is the central wavelength.

We model the sample, $\eta(z)$, as an ensemble of point scatterers:

$$\eta(z) = \sum_i^N R_i \delta(z - z_i), \quad (2)$$

where N is the total number of scatterers; R_i is the scatterer reflectivity; and $\delta(z - z_i)$ is the Dirac delta function at location z_i . A model for the initial (reference) OCT scan, $s_R(z)$, is:

$$s_R(z) = h(z) * \eta(z), \quad (3)$$

where $*$ denotes the convolution operation. If the sample undergoes an axial displacement, u_z , the resulting OCT scan of the displaced scatterers, $s_D(z)$ becomes:

$$s_D(z) = h(z) * \eta(z - u_z). \quad (4)$$

The phase difference, $\Delta\phi$, between Eqs. (3) and (4) can be calculated from the Kasai estimator [46]:

$$\Delta\phi = \angle \overline{s_R(z)} s_D(z) = \angle [\overline{h(z) * \eta(z)}][h(z) * \eta(z - u_z)], \quad (5)$$

where $\overline{s_R(z)}$ represents the complex conjugate of $s_R(z)$. In this model, a specular reflector can be treated as a single scatterer with reflectivity R_0 , and location z_0 . The corresponding phase difference is given by:

$$\begin{aligned} \Delta\phi &= \angle R_0 \overline{h(z_0)} R_0 h(z_0 - u_z) \\ &= \angle R_0^2 A_0^2 \exp \left\{ -2 \left[\frac{z_0^2}{w_z^2} + \frac{(z_0 - u_z)^2}{w_z^2} \right] \right\} \exp(2ik_0 u_z), \\ &= 2k_0 u_z \end{aligned} \quad (6)$$

Equation (6) can be rearranged to express u_z in terms of the phase difference and λ_0 , which yields the commonly used equation for axial displacement in phase-sensitive OCT [12]:

$$u_z = \frac{\Delta\phi \lambda_0}{4\pi n}, \quad (7)$$

sample refractive index, n , has been added to convert optical path length to physical distance. However, in turbid samples, the sample will typically contain many single scattering events within the PSF resolution, resulting in speckle, so applying Eq. (7) to the Kasai estimator between the reference and displaced samples only yields an approximation to u_z .

In Fig. 1, we illustrate the degradation in accuracy caused by speckle when using this model by simulating three scenarios. In each scenario, the sample is translated a known distance (corresponding to a known phase difference), and the measured phase difference is compared to the known phase difference to characterize accuracy. Firstly, in Fig. 1(a), we translate a single scatterer to represent a specular reflection. Secondly, in Fig. 1(b), we translate five scatterers, arranged to generate mostly constructive interference to represent bright speckle. Thirdly, in Fig. 1(c), we translate five scatterers, arranged to generate mostly destructive interference to represent dark speckle. We show the physical scatterer locations and corresponding OCT intensity in each case. We define the PSF in Eq. (1) with $A_0 = 1$; a full width at half maximum (FWHM) axial resolution = $4.8 \mu\text{m}$ ($w_z = 4.8/\sqrt{\ln(2)}$); and $\lambda_0 = 1.3 \mu\text{m}$ to match the experimental conditions that are described in Section 3.2. In all cases, $R_i = 1$, and each scatterer is translated by $0.325 \mu\text{m}$, corresponding to a π radians phase difference through Eq. (7). The phasor representations of the OCT signals evaluated at $z = 0$ (denoted by the vertical dotted gray lines in Figs. 1(a), 1(b) and 1(c)) for both the reference and translated scatterers are shown for the specular reflection,

bright speckle, and dark speckle cases, in Figs. 1(d), 1(e) and 1(f), respectively. The phase difference between the reference and translated OCT signal in the single scatterer case is π , *i.e.*, 0% error, as expected, given the absence of noise in this model. However, in the bright speckle case (Fig. 1(e)), the phase difference is ~ 3.12 radians, corresponding to an error of ~ 0.02 radians, or $\sim 0.6\%$. In dark speckle (Fig. 1(f)), the phase difference is ~ 2.50 radians, resulting in a larger error of ~ 0.64 radians, or $\sim 20.3\%$.

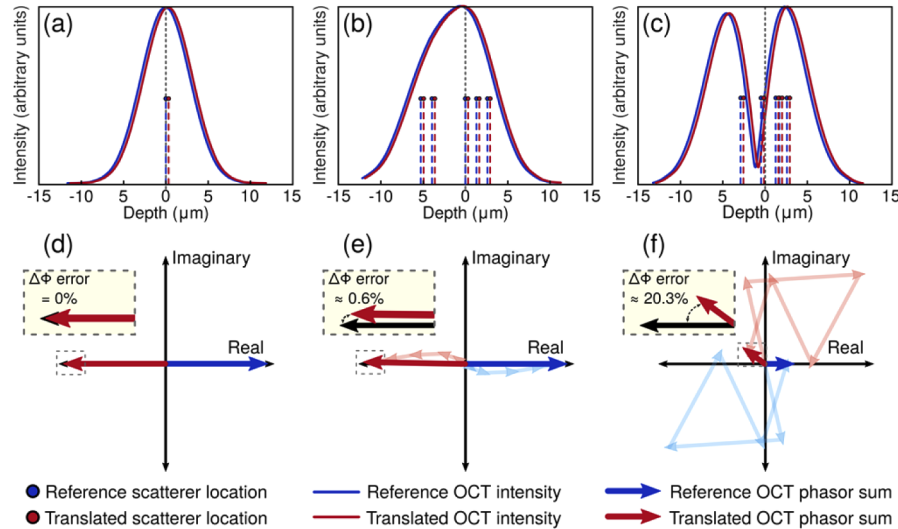


Fig. 1. The impact of speckle on the accuracy of phase-sensitive OCT. Reference and translated scatterer locations, and corresponding OCT intensity, of (a) a single scatterer (specular reflector), (b) five scatterers constructively interfering (bright speckle), and (c) five scatterers destructively interfering (dark speckle) undergoing a π radian phase shift. Phasor representations of the reference and translated OCT signals evaluated at $z = 0$ for (d) a single scatterer, (e) five scatterers in bright speckle, and (f) five scatterers in dark speckle.

In the speckle cases, Figs. 1(b) and 1(c), the phase measured at $z = 0$ comprises the complex summation of all scatterers, with their amplitudes being dependent on their relative distance from $z = 0$ in the PSF. The key to the inaccuracy arising from speckle is that displacement of the scatterers relative to $z = 0$ leads to a modulation in their amplitudes. Despite each individual phasor rotating by π radians, the total rotation of the phasor sum is not exactly π radians due to the change in amplitudes. Figure 1(e) suggests that even with strong constructive interference, where the signal closely resembles a specular reflection, there may still be an error. Figure 1(f) demonstrates that, in regions of destructive interference (dark speckle), as the contributions from each scatterer are initially cancelling each other out, small changes in amplitude significantly change the weighting of each scatterer in the final phase difference measurement. This significantly reduces the accuracy of the phase difference measurement in regions of dark speckle. In the following section, we demonstrate how this inaccuracy affects the probability distribution function (PDF) of phase difference measurements in speckle.

2.2. Impact of speckle inaccuracy on the phase difference distribution

In this section, we show that, due to the inaccuracy from speckle, the OCT SNR alone is insufficient to describe the PDF of phase difference in speckle. As optical noise varies temporally, its effect on the phase difference PDF can be characterized by acquiring multiple measurements in the same spatial location over time [40]. The analysis in Section 2.1, consistent with existing literature, suggests that phase difference measured in a specular reflection is accurate. That is,

the noise distribution of the phase difference caused by OCT SNR is zero-mean. Therefore, in a specular reflection, provided the system is shot-noise limited, and the OCT SNR $\gg 1$, the phase difference PDF should closely follow a Gaussian distribution around the true mean with a standard deviation, $\sigma_{\Delta\phi}$, given by the approximation [47]:

$$\sigma_{\Delta\phi} = \frac{1}{\sqrt{SNR}}. \quad (8)$$

In this case, the phase difference PDF is dependent only on the OCT SNR. A problem associated with extrapolating Eq. (8) to speckle is that, as described in Section 2.1, speckle introduces a fundamental inaccuracy to phase difference measurements. We show that the inaccuracy from speckle is unbiased by comparing the mean value of experimental measurements between a specular reflection and speckle in Section 1 of Supplement 1. Importantly, the inaccuracy for a single realization is temporally invariant. Therefore, whilst the phase difference distribution in a specular reflection, and a single speckle realization, is characterized by the OCT SNR (Eq. (8)), the inaccuracy in speckle will broaden the distribution of phase difference measured in multiple, independent, speckle realizations. This concept is illustrated below in Fig. 2 for several speckle realizations with the same OCT SNR.

In Fig. 3, we show the effect of speckle on the phase difference PDF. As the approximation in Eq. (8) is based on a phasor with a given noise distribution, it does not matter whether the cluster of phasors are measured from the same location over time, or from multiple locations at the same time [47]. We can therefore analyze the distribution of phase difference between points with the same OCT SNR from different speckle realizations. We measure the phase difference in pixels at the same location between two consecutive B-scans. In Fig. 3, in both simulation and experiment, we plot histograms of phase difference for three cases: (1) the same spatial location over time in a specular reflection; (2) the same spatial location over time in speckle; and (3) different spatial locations in speckle, each with the same OCT SNR. Detailed descriptions of the simulation and experiment setup are provided in Sections 3.1 and 3.2, respectively. In Fig. 3, in each case, we analyze 200 measurements with an effective OCT SNR of 20 ± 1 dB. The effective OCT SNR (ESNR) was calculated using the approach developed previously [43]:

$$ESNR = [(1 + SNR_1^{-1})(1 + SNR_2^{-1}) - 1]^{-1}. \quad (9)$$

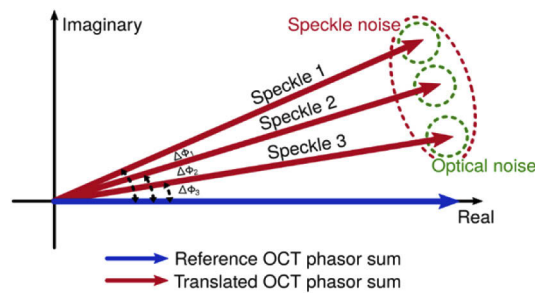


Fig. 2. Illustration of the impact of speckle inaccuracy on the phase difference distribution for multiple, independent, speckle realizations. The green dotted lines represent the distribution of the OCT signal based on optical noise. The red dotted lines represent the distribution of the OCT signal based on optical noise and speckle.

The red curves in Fig. 3 are Gaussian PDFs with $\sigma_{\Delta\phi} = 0.01$ predicted using Eq. (8) for an OCT SNR of 20 dB. The mean was subtracted from each histogram to compare each case more clearly. In Figs. 3(a) and 3(d), in simulation and experiment, respectively, we show the phase difference

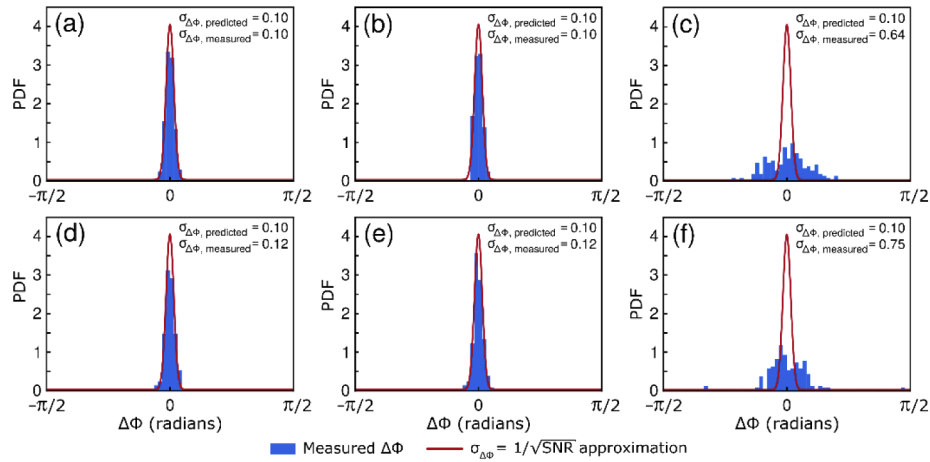


Fig. 3. Histograms of 200 phase difference measurements with an effective OCT SNR of 20 ± 1 dB acquired in (a), (d) a single spatial location in a specular reflection over time; (b), (e) a single spatial location in speckle over time; and (c), (f) independent speckle realizations. (a)–(c) are from simulation and (d)–(f) are from experiment.

histograms from the same spatial location over time in a specular reflector. As expected, in both cases, the standard deviation closely matches the prediction of Eq. (8). The slightly larger standard deviation in experiment compared to simulation is attributed to mechanical noise from translating the sample and from laterally scanning the OCT beam. In Figs. 3(b) and 3(e), in simulation and experiment, respectively, we show the phase difference histogram from the same spatial location over time in speckle. Here, as the speckle realization remains fixed, we are effectively measuring the impact of optical noise. As expected, in both cases, the standard deviation also closely matches the prediction of Eq. (8). In Figs. 3(c) and 3(f), in simulation and experiment, respectively, we show the phase difference histograms from independent speckle realizations, with each measurement having the same OCT SNR. Here, we can clearly see that the measured standard deviation is significantly greater than that predicted from Eq. (8). This suggests that OCT SNR alone is insufficient to describe the phase difference standard deviation in speckle. Whilst the inaccuracy introduced by speckle appears to be zero-mean, it manifests as a degradation to phase difference sensitivity. Like Section 2.1, this effect is likely to be worse in dark speckle where the phasors are destructively interfering. In the following sections, we introduce a metric to quantify the degree of constructive interference at a given location in speckle, speckle brightness, and study the relationship between speckle brightness and phase difference sensitivity.

3. Methods

3.1. Simulation

To extend the model described in Section 2.1 to account for the attenuation of samples, we scale the scatterer magnitudes according to the Beer-Lambert law [48–50], which states that the backscattered OCT intensity, $I(z)$, as a function of depth, z , is proportional to the reflectance, $R(z) = \rho \exp(-2\mu_t z)$ where ρ and μ_t are the backscattering and attenuation coefficients, respectively [51]. Values of $\rho = 0.074$ and $\mu_t = 0.003 \text{ mm}^{-1}$, were chosen to match experimental conditions, detailed in Section 3.2. The density of scattering potentials was ~ 5 per OCT axial resolution (FWHM) to ensure a fully developed speckle pattern [52]. The OCT intensity FWHM = $4.8 \mu\text{m}$ ($w_z = 4.8/\sqrt{\ln(2)}$); $\lambda_0 = 1.3 \mu\text{m}$ $A_0 = 1$; and optical noise was simulated by adding complex

Gaussian white noise with variance, $\sigma^2 = 0.0008$, to match the OCT SNR in experiment. Sample translation was modeled by adding a displacement to the scatterer locations. Phase difference was evaluated between complex OCT A-scans of the reference and displaced scatterer locations. 255 million phase difference measurements are analyzed in simulation in each case in Sections 4.1,4.2.

3.2. Experiment procedure

To provide experimental validation of the simulation, a homogeneous phantom and a phantom containing a stiff inclusion were fabricated using Elastosil silicone elastomers [53] with controlled optical and mechanical properties. The phantoms were 3 mm thick cylinders with diameters of 15 mm. The mechanical properties were controlled by selecting different elastomers and varying the ratio of the catalyst, curing agent and silicone oil. The stress-strain relationship of each silicone was characterized using a custom-built uniaxial compression testing apparatus as detailed previously [54]. The stiffnesses of the bulk in both phantoms was 21 kPa, and the stiffness of the inclusion, was 625 kPa, measured at 15% strain. The inclusion was fabricated as a rectangular prism with a cross-sectional geometry of $250 \times 250 \mu\text{m}$ and a length of 10 mm. The optical scattering properties were controlled by evenly mixing titanium dioxide particles (Sigma-Aldrich, Germany) (mean diameter $\sim 1 \mu\text{m}$) into the silicone. The concentration of scatterers in the homogeneous phantom was 10 mg/ml. The concentration of scatterers in the inclusion phantom were 0.5 mg/ml in the bulk and 2.5 mg/ml in the inclusion to obtain good optical contrast.

Phase-sensitive OCT measurements were performed using a fiber-based spectral domain OCT system (Telesto 220, Thorlabs Inc., USA). The light source is a superluminescent diode with $\lambda_0 = 1300 \text{ nm}$ and a 3-dB spectral bandwidth of 170 nm. The measured axial resolution in air is $4.8 \mu\text{m}$ (FWHM). The scan lens (LSM03, Thorlabs Inc., USA) has a measured lateral resolution in air of $7.2 \mu\text{m}$ (FWHM). In each case, the sample was placed below a 65 mm diameter imaging window (Edmund Optics Inc., USA), where the imaging window is fixed to a ring actuator (Piezomechanik GmbH, Germany). The system was operated in common-path where the imaging window itself, a partial reflector, acted as the reference reflection. For the results in Sections 4.1,4.2, for the case of translation, the sample was placed with an air gap separating the sample and the imaging window at a five-degree angle from normal to the imaging window surface to remove unwanted reflections from the air/sample interface. To introduce displacement, the sample was kept stationary and the reference reflector (imaging window) was translated by applying a voltage to the ring actuator. An illustration of this setup is shown in Fig. 4(a). For the results in Sections 4.3–4.4, to perform compression OCE, the sample was placed normal to the imaging window, and a 15% bulk strain was applied using a motorized translation stage to ensure uniform contact between the rigid plate, phantom, and imaging window. Silicone oil was used to lubricate the sample boundaries. The imaging window, fixed to the ring actuator, transfers the compressive load to the phantom. Local axial strain is calculated from the gradient of axial displacement with depth using 1-D weighted-least squares (WLS) linear regression [13]. The OCE setup is illustrated in Fig. 4(b).

In all cases, the ring actuator was driven by a 10 Hz square wave synchronized with the B-scan acquisition such that the B-scans in each pair were acquired at different translation/compression levels. One B-scan pair was acquired at each lateral y -location and phase difference was calculated between the B-scans in each pair. In Sections 4.1–4.3, scans comprised 1000 A-scans per B-scan and 1000 B-scan pairs per volume over a $1 \times 1 \text{ mm}$ (x,y) field of view. Assuming a group refractive index of $n = 1.4$, the resulting (x,y,z) voxel size was $1 \times 1 \times 2.5 \mu\text{m}$. In Section 4.4, scans comprised 2000 A-scans per B-scan and 2000 B-scan pairs per volume over a $5 \times 5 \text{ mm}$ (x,y) field of view, resulting in an (x,y,z) voxel size of $2.5 \times 2.5 \times 2.5 \mu\text{m}$.

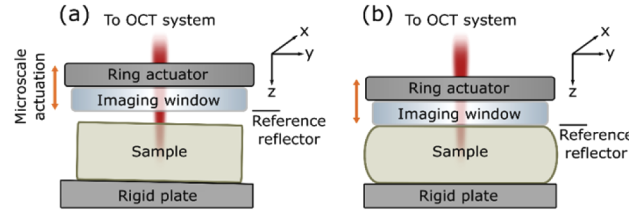


Fig. 4. Phase-sensitive OCT experiment setup. Illustrations of the experiments for (a) translating the sample, and (b) compression OCE.

3.3. Speckle brightness

From Section 2, speckle brightness, *i.e.*, the amount of constructive interference in the OCT signal, can vary from zero (fully dark speckle), to fully constructive (fully bright speckle). Therefore, we want to quantify speckle brightness to investigate its effect on phase difference. An intuitive approach to measure speckle brightness is to compare the measured OCT amplitude to the maximum possible amplitude at each spatial location. The maximum OCT amplitude in speckle can be determined in simulation by convolving the distribution of scatterers with the OCT point-spread function (PSF) envelope, *i.e.*, by ignoring the phase of the constituent responses. In this case, speckle brightness can be quantified by dividing the measured OCT amplitude by the maximum possible amplitude, yielding a measure from 0 (darkest speckle) to 1 (brightest speckle). We describe this approach in simulation in Section 2 of Supplement 1. However, this approach is impractical outside of simulation as it requires prior knowledge of the exact location and reflectivity of each sub-resolution scatterer. To quantify the degree of interference in experiment, we instead propose a metric based on the normalized Rayleigh distribution. This metric does not provide a direct measure of the degree of constructive interference; however, it has the advantage of only requiring the total OCT signal, and hence can be applied when the exact location and reflectivity of the sample scatterers are unknown. We provide a comparison between the metrics in simulation and experiment in Section 2 of Supplement 1 and show a positive association between the two. Throughout the remainder of this paper, we refer to the method used in experiment simply as “speckle brightness”.

To define speckle brightness, we assume that there are three contributions to the OCT amplitude: speckle, attenuation, and optical noise. In a homogeneous sample, the total attenuation is assumed to be constant for a given depth, z . The OCT amplitude, $|S(z)|$, for a particular depth, resulting from speckle, can be treated as a random variable sampled from a Rayleigh distribution with spread parameter, α_z [47,52,55]. The maximum likelihood estimate of α_z at each depth is given by:

$$\alpha_z \approx \sqrt{\frac{1}{2N} \sum_{i=1}^N |S(z_i)|^2} \quad (10)$$

where N is the total number of measurements at a given depth, z_i . We can use α_z at each depth to normalize $|S(z_i)|$. Optical noise is modeled as zero-mean additive Gaussian white noise, whose statistics are independent of spatial location. For the purposes of speckle brightness, the primary influence of optical noise is to introduce noise into the measurements of $|S(z_i)|$, and hence of α_z . We define speckle brightness (SB) as the normalized OCT amplitude:

$$SB(z_i) = \frac{|S(z_i)|}{\alpha_z}. \quad (11)$$

Speckle brightness follows a normalized Rayleigh distribution (*i.e.*, with spread parameter equal to 1), and is theoretically in the range $[0, \infty]$ and practically $[0, 5]$ in the results shown in

Section 4. Speckle brightness is positively associated with OCT SNR, however there are still a wide range of speckle brightness values for any given OCT SNR, and vice versa.

In Fig. 5, we illustrate that points in an OCT image can have equivalent OCT SNRs, but different amounts of constructive interference. Figures 5(a) and 5(b) show OCT SNR, and speckle brightness, B-scans, respectively, of the homogeneous phantom. In Figs. 5(c) and 5(e), we show magnified views of the region denoted by the blue squares in Figs. 5(a) and 5(b). In these regions, speckle is clearly visible. As this region is close to the sample surface, little attenuation has occurred, and the average OCT SNR is high. In the magnified regions, the green arrows indicate an example location with an OCT SNR of ~ 25 dB, and low speckle brightness (~ 0.51), representing a region of dark speckle. In Figs. 5(d) and 5(f), we show magnified views of a region deeper into the sample denoted by the yellow squares in Figs. 5(a) and 5(b), respectively. In these magnified regions, the light blue arrows indicate an example location with an OCT SNR of ~ 25 dB and high speckle brightness (~ 4.25), representing bright speckle. This illustrates how regions of dark speckle, particularly towards the surface of a turbid sample, can still have a high OCT SNR. Whilst the points indicated by the arrows in Fig. 5 have the same OCT SNR, there is likely to be reduced accuracy and sensitivity in the dark speckle case. However, with the OCT SNR alone, the two locations cannot be distinguished. In the following section, we investigate the relationship between speckle brightness and phase difference sensitivity for points with equivalent OCT SNRs.

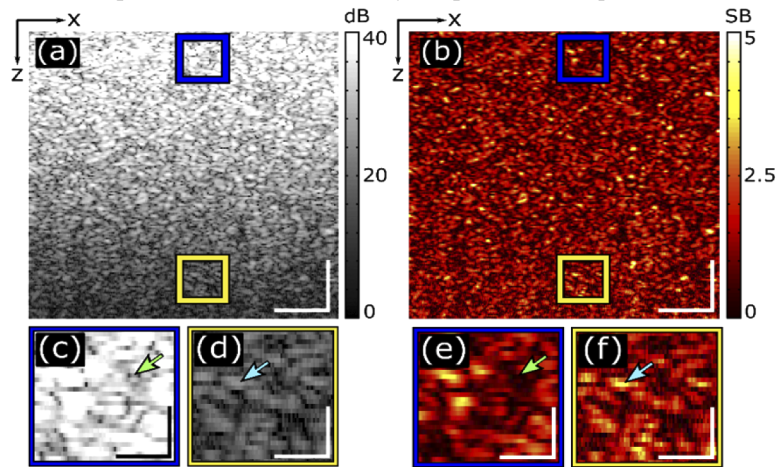


Fig. 5. OCT SNR (a) and speckle brightness (b) B-scans of a homogeneous phantom in experiment. (c) and (e) are magnified regions of the blue squares in (a) and (b), respectively. (d) and (f) are magnified regions of the yellow squares in (a) and (b), respectively. Green arrows indicate regions with an OCT SNR of 25 dB and low speckle brightness. Light blue arrows indicate regions with an OCT SNR of 25 dB and high speckle brightness. Scale bars represent $100\ \mu\text{m}$ in (a)–(b) and $20\ \mu\text{m}$ in (c)–(f).

4. Results

4.1. Fixed translation and different OCT SNRs

In Fig. 6, we show the relationship between phase difference sensitivity and speckle brightness for a turbid sample undergoing translation. In simulation and experiment, we translate a homogeneous phantom $1.3\ \mu\text{m}$ and compare points with the same OCT SNR and different speckle brightness. Figures 6(a)–6(c) show histograms of phase difference versus speckle brightness for points in simulation with an OCT SNR of 15 ± 1 dB, 20 ± 1 dB, and 25 ± 1 dB, respectively. Similarly, in

Figs. 6(d)–6(f), we show histograms of phase difference versus speckle brightness for points in experiment with an OCT SNR of 15 ± 1 dB, 20 ± 1 dB, and 25 ± 1 dB, respectively. The color scale in Fig. 6 represents the number of measurements in each histogram bin divided by the total number of measurements. Here, simulation and experiment are in close agreement. In each case, the phase difference distribution decreases in width as speckle brightness increases. This demonstrates that phase difference sensitivity degrades as speckle brightness decreases.

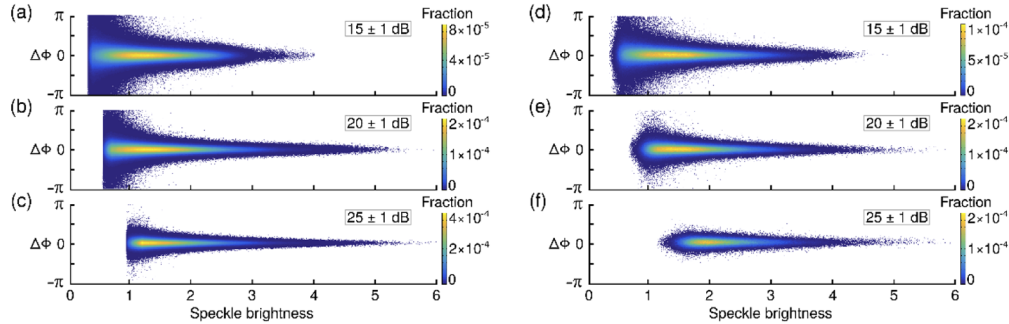


Fig. 6. Histograms of phase difference versus speckle brightness for points with an SNR of 15 ± 1 dB, 20 ± 1 dB, and 25 ± 1 dB in simulation (a)–(c), and experiment (d)–(f) for a fixed translation of $1.3 \mu\text{m}$ ($\Delta\phi = 4\pi$ radians).

In Fig. 7, we plot the standard deviation of phase difference as a function of speckle brightness at set OCT SNR values for the data presented in Fig. 6. The phase difference was binned in increments of 0.1 speckle brightness, and the standard deviation was computed for each bin. We set a criterion that each bin must contain at least 200 phase difference error measurements to minimize errors resulting from insufficient sampling, which resulted in plots with speckle brightness ranging from 1 to 5. The equivalent standard deviation in terms of displacement, σ_D , is also provided. In Fig. 7, the solid and dashed curves from simulation and experiment, respectively, are from measurements in speckle, while the red, blue, and yellow dot-dashed lines represent the expected sensitivity (Eq. (8)) for measurements in a specular reflection with an OCT SNR of 16 dB, 21 dB, and 26 dB, respectively. In each case, the phase difference standard deviation decreases with increasing speckle brightness and is greater than the expected standard deviation from the OCT SNR alone. For example, for points with an SNR of 20 ± 1 dB, sensitivity degrades from ~ 0.14 radians (~ 15 nm) to ~ 0.39 radians (~ 40 nm), corresponding to a ~ 2.67 times lower sensitivity between bright and dark speckle. In each case, the sensitivity begins to approximate that of a specular reflector for high speckle brightness.

4.2. Fixed OCT SNR and different translations

In Fig. 8, we demonstrate that phase difference sensitivity degrades with increasing translation and, furthermore that this degradation is more pronounced in dark speckle than in bright speckle. In simulation and experiment, we translate the homogeneous phantom $1.3 \mu\text{m}$, $2.3 \mu\text{m}$, and $3.9 \mu\text{m}$, corresponding to phase differences of 4π , 7π , and 12π , respectively. In each case, we analyze points with an OCT SNR of 20 ± 1 dB. Like Section 4.1, we compute the standard deviation of the phase difference error in bins in increments of 0.1 speckle brightness, with bin widths of 0.1, but only if there are at least 200 measurements in each bin. We plot the phase difference standard deviation as a function of speckle brightness for each translation. The equivalent standard deviation in terms of displacement, σ_D , is also provided. Here, simulation and experiment are in close agreement, and for each translation, sensitivity improves as speckle brightness increases from 1 to 4. In Fig. 8, the solid and dashed curves from simulation and experiment, respectively, are from measurements in speckle, while the black dot-dashed line

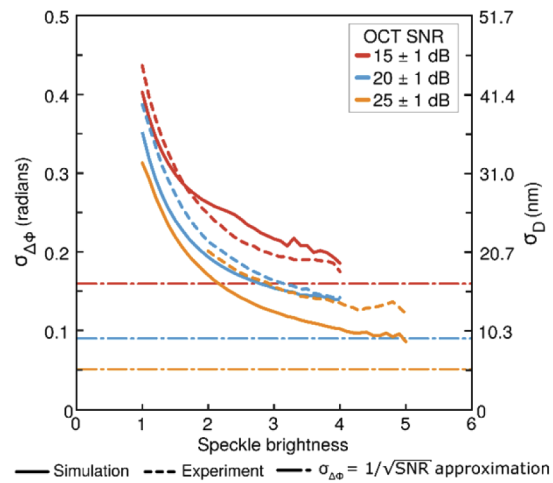


Fig. 7. Plots of phase difference standard deviation versus speckle brightness for measurements with OCT SNRs of 15 ± 1 dB, 20 ± 1 dB, and 25 ± 1 dB and a fixed translation of $1.3 \mu\text{m}$ ($\Delta\phi = 4\pi$ radians).

represents the expected sensitivity (Eq. (8)) for measurements in a specular reflection with an OCT SNR of 21 dB. Like Fig. 7, in each case, the phase difference standard deviation decreases with increasing speckle brightness and is greater than the expected standard deviation from the OCT SNR alone. As the translation increases, the curves shift upwards and the degradation in sensitivity is greater in dark speckle than in bright speckle. For example, for the $3.9 \mu\text{m}$ translation, phase difference sensitivity degrades from ~ 0.38 radians (~ 40 nm) to ~ 1.07 radians (~ 110 nm), corresponding to a ~ 2.85 times degradation in sensitivity between bright and dark speckle compared to the ~ 2.67 times degradation at a lower translation of $1.3 \mu\text{m}$.

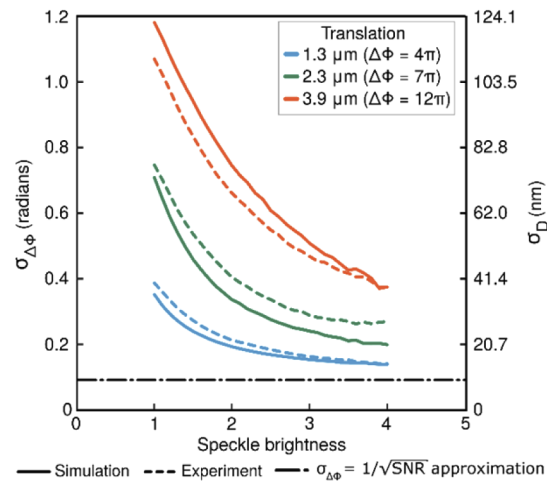


Fig. 8. Plots of phase difference standard deviation versus speckle brightness for translations of $1.3 \mu\text{m}$ ($\Delta\phi = 4\pi$ radians), $2.3 \mu\text{m}$ ($\Delta\phi = 7\pi$ radians) and $3.9 \mu\text{m}$ ($\Delta\phi = 12\pi$ radians) and a fixed OCT SNR of 20 ± 1 dB.

4.3. Improving strain sensitivity in OCE

In Fig. 9, we demonstrate how incorporating independent speckle realizations can improve strain sensitivity in compression OCE beyond what would be expected to result from an improvement in OCT SNR. In compression OCE, axial strain is typically estimated from the gradient of axial displacement versus depth over a sliding window of length 50–100 μm to alleviate the effect of noise [13]. One approach to reduce speckle and improve displacement (and strain) sensitivity is to spatially average B scan pairs in a homogenous sample. To illustrate this, in Fig. 9, we perform compression OCE on a homogeneous phantom and compare depth profiles from the center A-scan of an (x,z) B-scan generated using three approaches: (1) no averaging; (2) temporally averaging 100 B-scan pairs with the same speckle realizations; and (3) spatially averaging 100 B-scan pairs, acquired 10 μm apart, with independent speckle realizations. The mean OCT amplitude, OCT SNR, and phase difference are computed across pixels at the same B-scan location. The methods used to compute the mean OCT amplitude, OCT SNR and phase difference are described in detail in Section 3 of Supplement 1. A 1-D WLS strain fit length of 50 μm was used in all the results shown in Fig. 9. To first establish a baseline measurement, Figs. 9(a)–9(d) show depth profiles of the OCT SNR, speckle brightness (SB), displacement (D), and strain, respectively, of the center A-scan acquired from a single B-scan pair. As the sample is mechanically homogeneous, we would expect a constant rate of change in displacement, and hence a constant strain, with depth. However, due to optical noise and speckle, we instead observe a large variation in strain.

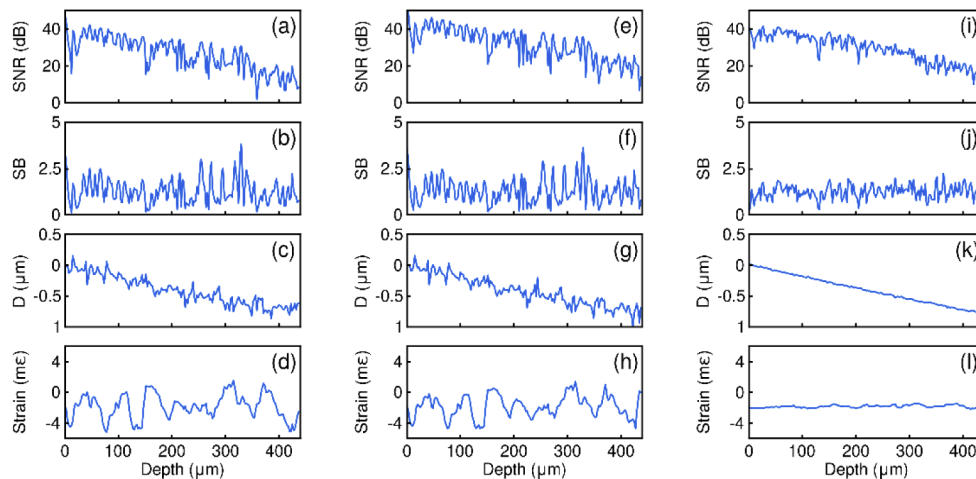


Fig. 9. Effect of averaging independent speckle patterns on strain estimation. (a) OCT SNR, (b) speckle brightness, (c) displacement, and (d) strain A-scans made with no averaging. (e) OCT SNR, (f) speckle brightness, (g) displacement, and (h) strain A-scans made by averaging 100 A-scan pairs with the same speckle pattern. (i) OCT SNR, (j) speckle brightness, (k) displacement, and (l) strain A-scans made by averaging 100 A-scan pairs with independent speckle patterns.

To demonstrate the effect of temporally averaging the same speckle realizations, Figs. 9(e)–9(h) show depth profiles of the OCT SNR, speckle brightness, displacement, and strain, respectively, of the center A-scan of a B-scan generated by temporally averaging 100 B-scan pairs. These depth profiles are acquired in the same spatial location as those presented in Figs. 9(a)–9(d). In the temporal averaging case, there is a slight increase in OCT SNR. However, the distribution of bright and dark speckle in the speckle brightness profile in Fig. 9(f) remains largely unchanged. Whilst temporal averaging reduces the effect of optical noise, the displacement measurements in

dark speckle remain constrained around an inaccurate mean value. Hence, there is negligible improvement in displacement and strain sensitivity.

To demonstrate the effect of averaging independent speckle realizations, Figs. 9(i)–9(l) show depth profiles of the OCT SNR, speckle brightness, displacement, and strain, respectively, of the center A-scan of a B-scan generated by spatially averaging 100 B-scan pairs, acquired 10 μm apart, with independent speckle realizations. Importantly, we average the same number of optical noise realizations as in the temporal averaging case, such that any observed difference is due to averaging the effect of speckle. In the spatial averaging case, we observe a homogenization of speckle brightness with depth. Consequently, we observe a significant improvement in both displacement and strain sensitivity in Figs. 9(k) and 9(l), respectively, compared to the temporal averaging case.

In Table 1, we quantify the improvement in strain sensitivity for both averaging methods. In each case, strain sensitivity is computed as the standard deviation of 200 strain measurements along the x -dimension at a constant depth. Strain sensitivity is computed at three depths: 125 μm , 250 μm and 375 μm . The results in Table 1 show that temporal averaging leads to a negligible improvement in strain sensitivity at each depth. In comparison, averaging independent speckle realizations leads to a ten-fold improvement in strain sensitivity at depths of 125 μm and 250 μm and an eight-fold increase at 375 μm .

Table 1. The effect of different averaging methods on strain sensitivity.

Depth (μm)	Strain sensitivity (mε)		
	No averaging	Temporally averaging 100 B-scan pairs	Spatially averaging 100 B-scan pairs
125	1.40	1.39	0.14
250	1.64	1.61	0.16
375	1.83	1.75	0.23

4.4. Improving contrast-to-noise in OCE

In Fig. 10, we demonstrate how incorporating independent speckle realizations can improve the contrast-to-noise ratio (CNR) in compression OCE, as shown in an inclusion phantom. The inclusion has a square cross section and was fabricated as a long rectangular prism in the y -dimension. Therefore, we can average independent speckle realizations by spatially averaging along the y -dimension. In Section 4.3, we demonstrated how temporal averaging does little to improve strain sensitivity when averaging the same speckle pattern. Therefore, in Fig. 10, we only compare two cases: (1) no averaging; and (2) spatially averaging 100 B-scan pairs with independent speckle patterns. A strain fit length of 50 μm was used in both cases. Figures 10(a) and 10(b) show an (x,z) OCT B-scan, and strain elastogram, respectively, of the inclusion phantom generated with no averaging. Figures 10(c) and 10(d) show an (x,z) OCT B-scan and strain elastogram, respectively, of the inclusion phantom generated by spatially averaging 100 B-scan pairs.

The strain CNR was computed using an approach used previously [56]:

$$CNR = \frac{|\mu_{\text{inc}} - \mu_{\text{bulk}}|}{\sqrt{\sigma_{\text{inc}}^2 + \sigma_{\text{bulk}}^2}}, \quad (12)$$

where μ_{inc} and μ_{bulk} are the mean strain values taken from a $200 \times 200 \mu\text{m}$ region in the inclusion and bulk respectively, and σ_{inc} and σ_{bulk} are the standard deviations of the strain measurements in each of the corresponding regions. The CNR measured in Fig. 10(b) was 0.93. Averaging multiple independent speckle realizations decreases speckle contrast [57] to improve the ability

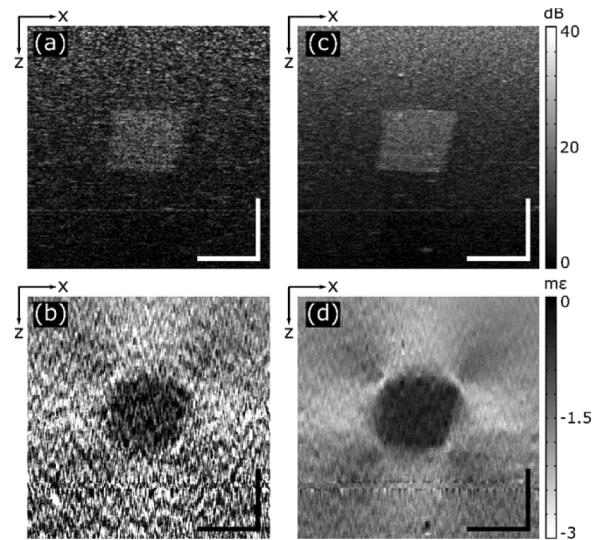


Fig. 10. The effect of averaging independent speckle realizations on strain elastograms of an inclusion phantom. (a) OCT SNR and (b) strain elastogram of an inclusion phantom generated with no averaging. (c) OCT SNR and (d) strain elastogram of the same inclusion phantom generated by averaging 100 B-scan pairs with independent speckle realizations. Scale bars represent 250 μm .

to distinguish the inclusion in the OCT SNR in Fig. 10(c), and the measured CNR in Fig. 10(d) was 4.67, representing a greater than five-fold increase in strain CNR.

5. Discussion

In this study we have presented, for the first time, the mechanism by which speckle affects the accuracy of phase-sensitive OCT beyond that predicted from the OCT SNR alone. The relationship between phase and displacement is assumed to be linear, which is valid for a specular reflector. However, in speckle, the relationship between phase and displacement becomes non-linear, reducing accuracy, where this effect worsens in regions of destructive interference (*i.e.*, dark speckle). In this study, we have shown how this effect can be modeled using a PSF with a linear phase field where the addition of phasors from multiple scatterers sums to a non-linear relation between phase and displacement. This deleterious effect of speckle has prevented the exceptional phase-sensitivity of OCT to be experimentally realized in turbid tissues. In fact, several previous studies have observed some form of this phenomenon. For example, in Doppler OCT, Walter and Koch reported “phase cancellation” at combinations of axial and lateral motion when the intensity of the backscattered signal was still high [58]. In addition, in compression OCE, Zaitsev *et al.* described decorrelation of the OCT signal due to sub-pixel shifts of scatterers between loaded and unloaded OCT scans which caused artificially low estimates of local sample strain [59]. Here, we have demonstrated that these errors are likely to be present in any phase-sensitive detection scheme which exhibits speckle and arise from the changes in the relative weighting of each of scatterer during motion. This will impact image quality in turbid media, including most biological tissues, and should be carefully considered when designing detection and computational schemes.

The results in Section 4 show, that due to speckle, even points with high OCT SNR can be inaccurate. This is likely to affect image quality in many applications of phase-sensitive OCT,

including Doppler OCT and OCE, where the OCT SNR alone is typically used to both infer accuracy and sensitivity. For example, weighted averaging techniques are used to improve image quality in OCE [13], where the optimal weights are the inverse variance of the data points [60]. Accordingly, based on the approximation developed from a specular reflector in Eq. (8), the weights are chosen to be the OCT SNR. However, our results show that points with high OCT SNR and low speckle brightness will introduce a bias, reducing the efficacy of weighted averaging techniques, and hence reduce image quality. This is likely to be problematic in applications of optically heterogeneous samples such as the retina, cell cultures, and adipose [2]. It is important to note that if the fit length of displacement is small enough such that the effect of attenuation is negligible, such as reasonably uniform tissues, then any change in OCT SNR will predominately be from speckle. In such a case, it is unlikely to matter whether the displacement is weighted by either the OCT SNR or speckle brightness as the magnitude of the weights only matters within the fitting window.

In applications that naturally develop independent speckle patterns with multiple acquisitions, such as flow imaging [1], temporal averaging can be used to reduce the effect of speckle. However, in applications involving temporally invariant speckle patterns, such as many forms of OCE, the effect of speckle cannot be reduced by temporal averaging because measurements in dark speckle are constrained around an inaccurate mean value. The results in Sections 4.3 and 4.4 demonstrate a significant improvement in sensitivity and CNR in OCE with no loss in system resolution [61] by spatially averaging independent speckle realizations. Whilst this shows the potential improvement in image quality that can be obtained by incorporating independent speckle realizations, it is impractical in applications involving heterogeneous samples, such as tumor margin assessment [6–8] and mechanobiology [62–64]. Whilst many phase-sensitive OCT systems currently use temporal averaging to improve OCT SNR, our results suggest that a greater emphasis should be placed on developing systems that can produce independent speckle patterns with subsequent acquisitions, such as those extensively developed to achieve speckle reduction in OCT [65–67]. This is likely to improve image quality in applications involving temporally invariant speckle patterns.

Displacement accuracy in speckle can likely be improved by incorporating spatial averaging. For example, in this study, the Kasai estimator was used to estimate the displacement at a single pixel location. However, techniques such as Loupas's algorithm [68,69], which spatially average the OCT signal, may improve displacement accuracy by incorporating a greater number of independent speckle realizations. Similar improvement can be realized in strain. In Section 4, axial strain was computed as the gradient of axial displacement using 1-D WLS regression over a 50 μm axial fit length. Strain estimation techniques using three-dimensional (3-D) WLS fitting [63], and the vector method [70], have been demonstrated with improved strain sensitivity by incorporating independent speckle realizations in the lateral dimensions. However, lateral averaging will degrade the lateral resolution and likely reduce displacement and strain accuracy in regions of mechanical heterogeneity. A potential approach to improve image quality without lateral averaging is to weight measurements by speckle brightness. In the current implementations of WLS, displacement is weighted by the OCT SNR, and in the vector method, the OCT SNR is incorporated by performing averaging in the complex domain. However, as points with high OCT SNR can still be inaccurate, strain estimation algorithms that incorporate both the OCT SNR and speckle brightness will likely improve strain sensitivity. This presents a promising avenue to improve image quality in turbid samples in future studies.

The analysis of speckle in phase-sensitive OCT presented here relies on several assumptions that may limit its accuracy. For example, a single scattering OCT model was used, however in scans of a turbid sample, multiple scattering events can occur, which have been shown to distort flow measurements in Doppler OCT [71,72]. Incorporating multiple scattering events was outside of the scope of this study, and the results in Section 4 show good agreement between

simulation and experiment, indicating that our 1-D simulation was sufficient to illustrate the effect of speckle on phase difference accuracy. Furthermore, in volumetric scans of turbid samples, the speckle pattern exists as a 3-D quantity, and our simulations were an ensemble of A-scans. In addition, whilst the method to estimate speckle brightness in this study has the advantage of being applicable in experiment, it requires a homogeneous sample and does not provide a direct measure of the constructive interference at each location in the OCT scan. Incorporating multiple scattering events, 3-D sample models, and more accurate estimates of speckle brightness will likely improve the understanding of how speckle affects image quality in phase-sensitive OCT.

6. Conclusion

We have presented the first study that describes how speckle affects the accuracy of phase-sensitive OCT beyond the effects from the OCT SNR. We described how the impact of speckle on accuracy affects phase difference sensitivity, and we investigated the relationship between phase difference sensitivity and speckle brightness for several OCT SNRs and translations. In each case, the phase difference sensitivity was poorer than that predicted from the OCT SNR. This suggests that OCT SNR alone is insufficient to fully explain phase difference sensitivity in speckle and that speckle brightness is an important factor that should be considered when interpreting phase-sensitive OCT results. Furthermore, by incorporating independent speckle realizations, we demonstrated a ten-fold improvement in strain sensitivity and a five-fold improvement in CNR in compression OCE. The results from this study emphasize the importance of developing phase-sensitive OCT systems that can produce independent speckle patterns with subsequent acquisitions to improve image quality in turbid media.

Funding. Australian Research Council; Department of Health, Australian Government; Cancer Council Western Australia; Oncores Medical; The William and Marlene Schrader Trust of the University of Western Australia; Royal Society.

Disclosures. BFK: OncoRes Medical (F, I) and LC: OncoRes Medical (I).

Supplemental document. See [Supplement 1](#) for supporting content.

References

1. R. A. Leitgeb, R. M. Werkmeister, C. Blatter, and L. Schmetterer, "Doppler Optical Coherence Tomography," *Prog. Retin. Eye Res.* **41**, 26–43 (2014).
2. B. F. Kennedy, P. Wijesinghe, and D. D. Sampson, "The emergence of optical elastography in biomedicine," *Nat. Photonics* **11**(4), 215–221 (2017).
3. Y. Wang, A. Fawzi, O. Tan, J. Gil-Flamer, and D. Huang, "Retinal blood flow detection in diabetic patients by Doppler Fourier domain optical coherence tomography," *Opt. Express* **17**(5), 4061–4073 (2009).
4. Y. Wang, A. A. Fawzi, R. Varma, A. A. Sadun, X. Zhang, O. Tan, J. A. Izatt, and D. Huang, "Pilot Study of Optical Coherence Tomography Measurement of Retinal Blood Flow in Retinal and Optic Nerve Diseases," *Invest. Ophthalmol. Visual Sci.* **52**(2), 840–845 (2011).
5. M. Sehi, I. Goharian, R. Konduru, O. Tan, S. Srinivas, S. R. Sadda, B. A. Francis, D. Huang, and D. S. Greenfield, "Retinal Blood Flow in Glaucomatous Eyes with Single-Hemifield Damage," *Ophthalmology* **121**(3), 750–758 (2014).
6. B. F. Kennedy, R. A. McLaughlin, K. M. Kennedy, L. Chin, P. Wijesinghe, A. Curatolo, A. Tien, M. Ronald, B. Latham, C. M. Saunders, and D. D. Sampson, "Investigation of optical coherence microelastography as a method to visualize cancers in human breast tissue," *Cancer Res.* **75**(16), 3236–3245 (2015).
7. K. M. Kennedy, R. Zilkens, W. M. Allen, K. Y. Foo, Q. Fang, L. Chin, R. W. Sanderson, J. Anstie, P. Wijesinghe, A. Curatolo, H. E. I. Tan, N. Morin, B. Kunjuraman, C. Yeomans, S. L. Chin, H. DeJong, K. Giles, B. F. Dessauvage, B. Latham, C. M. Saunders, and B. F. Kennedy, "Diagnostic Accuracy of Quantitative Micro-Elastography for Margin Assessment in Breast-Conserving Surgery," *Cancer Res.* **80**(8), 1773–1783 (2020).
8. W. M. Allen, L. Chin, P. Wijesinghe, R. W. Kirk, B. Latham, D. D. Sampson, C. M. Saunders, and B. F. Kennedy, "Wide-field optical coherence micro-elastography for intraoperative assessment of human breast cancer margins," *Biomed. Opt. Express* **7**(10), 4139–4153 (2016).
9. Z. Chen, T. E. Milner, S. Srinivas, X. Wang, A. Malekafzali, M. J. C. van Gemert, and J. S. Nelson, "Noninvasive imaging of in vivo blood flow velocity using optical Doppler tomography," *Opt. Lett.* **22**(14), 1119–1121 (1997).
10. J. A. Izatt, M. D. Kulkarni, S. Yazdanfar, J. K. Barton, and A. J. Welch, "In vivo bidirectional color Doppler flow imaging of picoliter blood volumes using optical coherence tomography," *Opt. Lett.* **22**(18), 1439–1441 (1997).

11. X. J. Wang, T. E. Milner, and J. S. Nelson, "Characterization of fluid flow velocity by optical Doppler tomography," *Opt. Lett.* **20**(11), 1337–1339 (1995).
12. R. K. Wang, Z. Ma, and S. J. Kirkpatrick, "Tissue Doppler optical coherence elastography for real time strain rate and strain mapping of soft tissue," *Appl. Phys. Lett.* **89**(14), 144103 (2006).
13. B. F. Kennedy, S. H. Koh, R. A. McLaughlin, K. M. Kennedy, P. R. T. Munro, and D. D. Sampson, "Strain estimation in phase-sensitive optical coherence elastography," *Biomed. Opt. Express* **3**(8), 1865–1879 (2012).
14. B. F. Kennedy, R. A. McLaughlin, K. M. Kennedy, L. Chin, A. Curatolo, A. Tien, B. Latham, C. M. Saunders, and D. D. Sampson, "Optical coherence micro-elastography: mechanical-contrast imaging of tissue microstructure," *Biomed. Opt. Express* **5**(7), 2113–2124 (2014).
15. B. Braaf, K. A. Vermeer, K. V. Vienola, and J. F. de Boer, "Angiography of the retina and the choroid with phase-resolved OCT using interval-optimized backstitched B-scans," *Opt. Express* **20**(18), 20516–20534 (2012).
16. B. F. Kennedy, F. G. Malheiro, L. Chin, and D. D. Sampson, "Three-dimensional optical coherence elastography by phase-sensitive comparison of C-scans," *J. Biomed. Opt.* **19**(7), 076006 (2014).
17. Y. Zhao, Z. Chen, C. Saxer, S. Xiang, J. F. de Boer, and J. S. Nelson, "Phase-resolved optical coherence tomography and optical Doppler tomography for imaging blood flow in human skin with fast scanning speed and high velocity sensitivity," *Opt. Lett.* **25**(2), 114–116 (2000).
18. R. A. Leitgeb, L. Schmetterer, W. Drexler, A. F. Fercher, R. J. Zawadzki, and T. Bajraszewski, "Real-time assessment of retinal blood flow with ultrafast acquisition by color Doppler Fourier domain optical coherence tomography," *Opt. Express* **11**(23), 3116–3121 (2003).
19. S. Makita, Y. Hong, M. Yamanari, T. Yatagai, and Y. Yasuno, "Optical coherence angiography," *Opt. Express* **14**(17), 7821–7840 (2006).
20. B. J. Vakoc, R. M. Lanning, J. A. Tyrrell, T. P. Padera, L. A. Bartlett, T. Stylianopoulos, L. L. Munn, G. J. Tearney, D. Fukumura, R. K. Jain, and B. E. Bouma, "Three-dimensional microscopy of the tumor microenvironment in vivo using optical frequency domain imaging," *Nat. Med.* **15**(10), 1219–1223 (2009).
21. C. Blatter, E. F. J. Meijer, A. S. Nam, D. Jones, B. E. Bouma, T. P. Padera, and B. J. Vakoc, "In vivo label-free measurement of lymph flow velocity and volumetric flow rates using Doppler optical coherence tomography," *Sci. Rep.* **6**(1), 29035 (2016).
22. V. J. Srinivasan, S. Sakadžić, I. Gorczynska, S. Ruvinskaya, W. Wu, J. G. Fujimoto, and D. A. Boas, "Quantitative cerebral blood flow with Optical Coherence Tomography," *Opt. Express* **18**(3), 2477–2494 (2010).
23. X. Liang, V. Crecea, and S. A. Boppart, "Dynamic optical coherence elastography: a review," *J. Innov. Opt. Health Sci.* **03**(04), 221–233 (2010).
24. J. A. Mulligan, G. R. Untracht, S. N. Chandrasekaran, C. N. Brown, and S. G. Adie, "Emerging approaches for high-resolution imaging of tissue biomechanics with optical coherence elastography," *IEEE J. Sel. Top. Quantum Electron.* **22**(3), 246–265 (2016).
25. K. V. Larin and D. D. Sampson, "Optical coherence elastography – OCT at work in tissue biomechanics [Invited]," *Biomed. Opt. Express* **8**(2), 1172–1202 (2017).
26. R. K. Wang and A. L. Nuttall, "Phase-sensitive optical coherence tomography imaging of the tissue motion within the organ of Corti at a subnanometer scale: a preliminary study," *J. Biomed. Opt.* **15**(5), 056005 (2010).
27. S. S. Gao, P. D. Raphael, R. Wang, J. Park, A. Xia, B. E. Applegate, and J. S. Oghalai, "In vivo vibrometry inside the apex of the mouse cochlea using spectral domain optical coherence tomography," *Biomed. Opt. Express* **4**(2), 230–240 (2013).
28. A. L. Oldenburg, J. R. Gunther, and S. A. Boppart, "Imaging magnetically labeled cells with magnetomotive optical coherence tomography," *Opt. Lett.* **30**(7), 747–749 (2005).
29. V. Crecea, B. W. Graf, T. Kim, G. Popescu, and S. A. Boppart, "High Resolution Phase-Sensitive Magnetomotive Optical Coherence Microscopy for Tracking Magnetic Microbeads and Cellular Mechanics," *IEEE J. Sel. Top. Quantum Electron.* **20**(2), 25–31 (2014).
30. R. John, R. Rezaeipoor, S. G. Adie, E. J. Chaney, A. L. Oldenburg, M. Marjanovic, J. P. Haldar, B. P. Sutton, and S. A. Boppart, "In vivo magnetomotive optical molecular imaging using targeted magnetic nanoprobe," *Proc. Natl. Acad. Sci. U. S. A.* **107**(18), 8085–8090 (2010).
31. T. Akkin, D. P. Davé, J. I. Youn, S. A. Telenkov, H. G. Rylander, and T. E. Milner, "Imaging tissue response to electrical and photothermal stimulation with nanometer sensitivity," *Lasers Surg. Med.* **33**(4), 219–225 (2003).
32. D. C. Adler, S. W. Huang, R. Huber, and J. G. Fujimoto, "Photothermal detection of gold nanoparticles using phase-sensitive optical coherence tomography," *Opt. Express* **16**(7), 4376–4393 (2008).
33. M. Lapierre-Landry, A. Y. Gordon, J. S. Penn, and M. C. Skala, "In vivo photothermal optical coherence tomography of endogenous and exogenous contrast agents in the eye," *Sci. Rep.* **7**(1), 9228 (2017).
34. J. F. de Boer, C. K. Hitzenberger, and Y. Yasuno, "Polarization sensitive optical coherence tomography; a review [Invited]," *Biomed. Opt. Express* **8**(3), 1838–1873 (2017).
35. L. P. Hariri, D. C. Adams, M. B. Applegate, A. J. Miller, B. W. Roop, M. Villiger, B. E. Bouma, and M. J. Suter, "Distinguishing Tumor from Associated Fibrosis to Increase Diagnostic Biopsy Yield with Polarization-Sensitive Optical Coherence Tomography," *Clin. Cancer Res.* **25**(17), 5242–5249 (2019).
36. K. Otsuka, M. Villiger, S. K. Nadkarni, and B. E. Bouma, "Intravascular Polarimetry: Clinical Translation and Future Applications of Catheter-Based Polarization Sensitive Optical Frequency Domain Imaging," *Front. Cardiovasc. Med.* **7**, 146 (2020).

37. A. B. Badiru and L. Racz, *Handbook of Measurements: Benchmarks for Systems Accuracy and Precision* (CRC Press, 2018).
38. S. Yazdanfar, C. Yang, M. V. Sarunic, and J. A. Izatt, "Frequency estimation precision in Doppler optical coherence tomography using the Cramer-Rao lower bound," *Opt. Express* **13**(2), 410–416 (2005).
39. B. J. Vakoc, G. J. Tearney, and B. E. Bouma, "Statistical properties of phase-decorrelation in phase-resolved Doppler optical coherence tomography," *IEEE Trans. Med. Imaging* **28**(6), 814–821 (2009).
40. B. H. Park, M. C. Pierce, B. Cense, S. H. Yun, M. Mujat, G. J. Tearney, B. E. Bouma, and J. F. de Boer, "Real-time fiber-based multi-functional spectral-domain optical coherence tomography at 1.3 μm ," *Opt. Express* **13**(11), 3931–3944 (2005).
41. M. A. Choma, A. Ellerbee, and J. A. Izatt, "Ultrasensitive Phase-Resolved Imaging of Cellular Morphology and Dynamics," in *Optical Coherence Tomography: Technology and Applications*, W. Drexler and J. G. Fujimoto, eds., Biological and Medical Physics, Biomedical Engineering (Springer, 2008), pp. 757–785.
42. J. M. Schmitt, S. H. Xiang, and K. M. Yung, "Speckle in optical coherence tomography," *J. Biomed. Opt.* **4**(1), 95–106 (1999).
43. S. Makita, F. Jaillon, I. Jahan, and Y. Yasuno, "Noise statistics of phase-resolved optical coherence tomography imaging: single-and dual-beam-scan Doppler optical coherence tomography," *Opt. Express* **22**(4), 4830–4848 (2014).
44. J. M. Schmitt and A. Knüttel, "Model of optical coherence tomography of heterogeneous tissue," *J. Opt. Soc. Am. A* **14**(6), 1231 (1997).
45. K. Kurokawa, S. Makita, Y. J. Hong, and Y. Yasuno, "In-plane and out-of-plane tissue micro-displacement measurement by correlation coefficients of optical coherence tomography," *Opt. Lett.* **40**(9), 2153–2156 (2015).
46. C. Kasai, K. Namekawa, A. Koyano, and R. Omoto, "Real-Time Two-Dimensional Blood Flow Imaging Using an Autocorrelation Technique," *IEEE Trans. Sonics Ultrason.* **32**(3), 458–464 (1985).
47. J. W. Goodman, *Statistical Optics* (John Wiley & Sons, 2015).
48. J. M. Schmitt, A. Knüttel, and R. F. Bonner, "Measurement of optical properties of biological tissues by low-coherence reflectometry," *Appl. Opt.* **32**(30), 6032–6042 (1993).
49. F. J. van der Meer, D. J. Faber, D. M. B. Sassoon, M. C. Aalders, G. Pasterkamp, and T. G. van Leeuwen, "Localized measurement of optical attenuation coefficients of atherosclerotic plaque constituents by quantitative optical coherence tomography," *IEEE Trans. Med. Imaging* **24**(10), 1369–1376 (2005).
50. P. Gong, R. A. McLaughlin, Y. M. Liew, P. R. T. Munro, F. M. Wood, and D. D. Sampson, "Assessment of human burn scars with optical coherence tomography by imaging the attenuation coefficient of tissue after vascular masking," *J. Biomed. Opt.* **19**(2), 021111 (2013).
51. R. R. Rennie and J. L. Law, "Beer–Lambert law," in *A Dictionary of Chemistry*, R. Rennie and J. Law, eds. (Oxford University Press, 2016).
52. A. Curatolo, B. Kennedy, D. Sampson, and T. R. Hilman, "Speckle in optical coherence tomography," *Advanced Biophotonics* CRC Press (2014) pp. 212–277.
53. G. Lamouche, B. F. Kennedy, K. M. Kennedy, C. E. Bisaillon, A. Curatolo, G. Campbell, V. Pazos, and D. D. Sampson, "Review of tissue simulating phantoms with controllable optical, mechanical and structural properties for use in optical coherence tomography," *Biomed. Opt. Express* **3**(6), 1381–1398 (2012).
54. R. W. Sanderson, A. Curatolo, P. Wijesinghe, L. Chin, and B. F. Kennedy, "Finger-mounted quantitative micro-elastography," *Biomed. Opt. Express* **10**(4), 1760–1773 (2019).
55. J. W. Goodman, *Speckle Phenomena in Optics: Theory and Applications* (Roberts and Company Publishers, 2007).
56. R. W. Sanderson, Q. Fang, A. Curatolo, W. Adams, D. D. Lakhiani, H. M. Ismail, K. Y. Foo, B. F. Dessauvagie, B. Latham, C. Yeomans, C. M. Saunders, and B. F. Kennedy, "Camera-based optical palpation," *Sci. Rep.* **10**(1), 15951 (2020).
57. D. D. Duncan, S. J. Kirkpatrick, and R. K. Wang, "Statistics of local speckle contrast," *J. Opt. Soc. Am. A* **25**(1), 9 (2008).
58. J. Walther and E. Koch, "Transverse motion as a source of noise and reduced correlation of the Doppler phase shift in spectral domain OCT," *Opt. Express* **17**(22), 19698–19713 (2009).
59. V. Y. Zaitsev, A. L. Matveyev, L. A. Matveyev, G. V. Gelikonov, A. A. Sovetsky, and A. Vitkin, "Optimized phase gradient measurements and phase-amplitude interplay in optical coherence elastography," *J. Biomed. Opt.* **21**(11), 116005 (2016).
60. J. Fox, *Applied Regression Analysis, Linear Models, and Related Methods* (Sage Publications, Inc, 1997).
61. M. S. Hepburn, P. Wijesinghe, L. Chin, and B. F. Kennedy, "Analysis of spatial resolution in phase-sensitive compression optical coherence elastography," *Biomed. Opt. Express* **10**(3), 1496–1513 (2019).
62. W. J. Hadden, J. L. Young, A. W. Holle, M. L. McFetridge, D. Y. Kim, P. Wijesinghe, H. Taylor-Weiner, J. H. Wen, A. R. Lee, K. Bieback, B. N. Vo, D. D. Sampson, B. F. Kennedy, J. P. Spatz, A. J. Engler, and Y. S. Choi, "Stem cell migration and mechanotransduction on linear stiffness gradient hydrogels," *Proc. Natl. Acad. Sci.* **114**(22), 5647–5652 (2017).
63. M. S. Hepburn, P. Wijesinghe, L. G. Major, J. Li, A. Mowla, C. Astell, H. W. Park, Y. Hwang, Y. S. Choi, and B. F. Kennedy, "Three-dimensional imaging of cell and extracellular matrix elasticity using quantitative micro-elastography," *Biomed. Opt. Express* **11**(2), 867–884 (2020).

64. L. G. Major, A. W. Holle, J. L. Young, M. S. Hepburn, K. Jeong, I. L. Chin, R. W. Sanderson, J. H. Jeong, Z. M. Aman, B. F. Kennedy, Y. Hwang, D. W. Han, H. W. Park, K. L. Guan, J. P. Spatz, and Y. S. Choi, "Volume Adaptation Controls Stem Cell Mechanotransduction," *ACS Appl. Mater. Interfaces* **11**(49), 45520–45530 (2019).
65. O. Liba, M. D. Lew, E. D. SoRelle, R. Dutta, D. Sen, D. M. Moshfeghi, S. Chu, and A. de la Zerda, "Speckle-modulating optical coherence tomography in living mice and humans," *Nat. Commun.* **8**(1), 1–13 (2017).
66. M. Pircher, E. Götzinger, R. A. Leitgeb, A. F. Fercher, and C. K. Hitzenberger, "Speckle reduction in optical coherence tomography by frequency compounding," *J. Biomed. Opt.* **8**(3), 565–569 (2003).
67. B. F. Kennedy, T. R. Hillman, A. Curatolo, and D. D. Sampson, "Speckle reduction in optical coherence tomography by strain compounding," *Opt. Lett.* **35**(14), 2445–2447 (2010).
68. T. Loupas, J. T. Powers, and R. W. Gill, "An axial velocity estimator for ultrasound blood flow imaging, based on a full evaluation of the Doppler equation by means of a two-dimensional autocorrelation approach," *IEEE Trans. Ultrason., Ferroelect., Freq. Contr.* **42**(4), 672–688 (1995).
69. D. Morofke, M. C. Kolios, I. A. Vitkin, and V. X. D. Yang, "Wide dynamic range detection of bidirectional flow in Doppler optical coherence tomography using a two-dimensional Kasai estimator," *Opt. Lett.* **32**(3), 253–255 (2007).
70. A. L. Matveyev, L. A. Matveev, A. A. Sovetsky, G. V. Gelikonov, A. A. Moiseev, and V. Y. Zaitsev, "Vector method for strain estimation in phase-sensitive optical coherence elastography," *Laser Phys. Lett.* **15**(6), 065603 (2018).
71. J. Kalkman, A. V. Bykov, D. J. Faber, and T. G. van Leeuwen, "Multiple and dependent scattering effects in Doppler optical coherence tomography," *Opt. Express* **18**(4), 3883–3892 (2010).
72. J. Kalkman, A. V. Bykov, G. J. Streekstra, and T. G. van Leeuwen, "Multiple scattering effects in Doppler optical coherence tomography of flowing blood," *Phys. Med. Biol.* **57**(7), 1907–1917 (2012).